

Frustrated Rydberg Atom Arrays Meet Cavity-QED: Emergence of the Superradiant Clock Phase

Ying Liang,¹ Bao-Yun Dong,¹ Zi-Jian Xiong,² and Xue-Feng Zhang^{1,3,*}

¹Department of Physics, and Chongqing Key Laboratory for Strongly Coupled Physics, Chongqing University, Chongqing, 401331, China

²College of Physics and Electronic Engineering, Chongqing Normal University, Chongqing 401331, China

³Center of Quantum Materials and Devices, Chongqing University, Chongqing 401331, China

Rydberg atom triangular arrays in an optical cavity serve as an ideal platform for understanding the interplay between geometric frustration and quantized photons. Using a large-scale quantum Monte Carlo method, we obtain a rich ground state phase diagram. Around half-filling, the infinite long-range light-matter interaction lifts the ground state degeneracy, resulting in a novel order-coexisted superradiant clock phase that completely destroys the fragile order-by-disorder phase observed in classical light fields. According to the Ginzburg-Landau theory, this replacement may result from the competition between threefold and sixfold clock terms. Similar to the spin supersolid, the clear first-order phase transition at the Z_2 symmetry line is attributed to the nonzero photon density, which couples to the threefold clock term. Finally, we discuss the low-energy physics in the dimer language and propose that cavity-mediated nonlocal ring exchange interactions may play a critical role in the rich physics induced by the attachment of cavity-QED. Our work opens a new arena of research on the emergent phenomena of quantum phase transitions in many-body quantum optics.

Introduction.— Matter coupled with light forms a key platform in quantum optics, where infinite long-range interactions give rise to a variety of exotic phenomena [1, 2], particularly quantum phase transitions (QPTs) [3–5]. Recent advancements, driven by the inclusion of additional degrees of freedom, have led to significant progress in understanding QPTs in light-matter quantum few-body systems, including phenomena such as multi-criticality [6, 7] and quantum magnetic clusters [8–10]. On the other hand, the integration of quantum many-body systems with cavity-QED [11–16] has begun to reshape our understanding of emergent phenomena and critical behavior in strongly interacting many-body quantum optics [2, 17].

Quantum frustration has garnered significant attention due to its abundance of exotic emergent phenomena, such as supersolid (SS) [18–21], emergent lattice gauge theory [22–25], quantum spin liquid [26–28], and deconfined criticality [29–35]. A characteristic example is the antiferromagnetic Ising model on a triangular lattice, where the competition between antiferromagnetic interactions and geometric frustration leads to a disordered ground state with high macroscopic degeneracy [36]. Interestingly, even infinitesimal quantum fluctuations can lift this degeneracy and result in an ordered ground state [20, 37, 38]. This phenomenon, known as the order-by-disorder (OBD) mechanism, is a representative example of the emergent behavior in such systems [39].

Recent advancements in Rydberg atom arrays have provided an ideal platform for simulating strongly correlated two-level atoms with exceptional tunability [41, 42]. The strongly interactive Rydberg atoms can be effectively mapped onto the extended transverse field Ising model (TFIM), in which the Rabi frequency Ω plays as a transverse field [43, 44]. By arranging tweezer sites with frustrated geometry, the interplay between frustration and the classical light field exhibits various exotic emergent phenomena, including not only the OBD phase [45], but also the spin liquid [46], spin glass [47, 48],

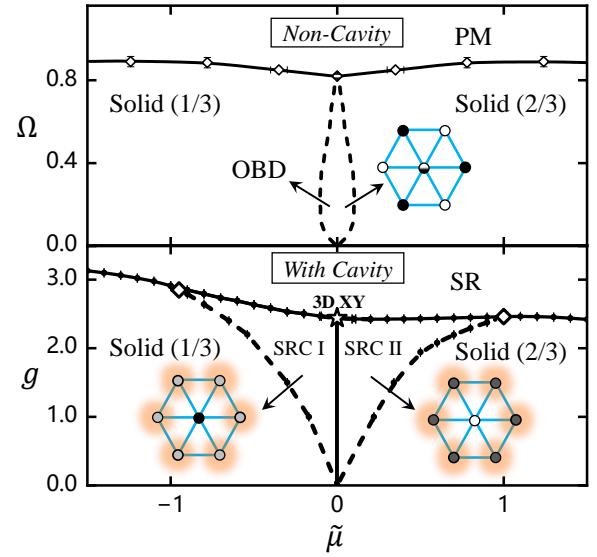


FIG. 1. Quantum phase diagrams of Rydberg atom arrays with or without a cavity. *Top:* The non-cavity phase diagram is obtained from Ref. [40] by transferring the parameters of the TFIM. *Bottom:* The phase diagram in a cavity is calculated by QMC simulation at $\Delta = 9$, where $\tilde{\mu} = \mu_b - 3V$. The dashed (solid) lines mark the second (first)-order phase transition. The diamond points represent the two triple points, and the star point labels the 3D XY critical point. The schematic pictures of the OBD phase and SRC phases are pointed with the black arrows.

and string breaking [49, 50]. Therefore, coupling a frustrated Rydberg atom array with an optical cavity [51–54] is expected to offer novel insights into emergent physics through the interplay among geometric frustration, strong Rydberg interaction, and the quantized photonic field.

In this manuscript, we investigate the frustrated Rydberg atom arrays coupled with quantized photonic fields by using a large-scale quantum Monte Carlo (QMC) simulation. Distinctively from the classical photonic field, as demonstrated in Fig. 1, the physics of OBD mechanisms is strongly enriched by the attachment of the cavity. Assisted by the infinite long-

* corresponding author: zhangxf@cqu.edu.cn

range light-matter interaction, a novel order coexisted phase named the superradiant clock (SRC) phase emerges and completely ruins the fragile OBD phase without a cavity. Different from the OBD phase with sixfold clock order, the SRC phase is driven by the threefold clock term reminiscent of the spin SS [20, 55–58]. Similar to the SS phases, the condensation also happens in the honeycomb backbone and the QPT to the disordered phase exhibits exotic criticality behaviors. However, in contrast to the mist of QPT between SS phases at zero magnetic field, two SRC phases undergo a clear first-order QPT. It hints the photon-induced particle-hole symmetry breaking strongly enhances the threefold clock term to being relevant. At last, according to the analysis of dimer representation, we think the nonlocal ring exchange interaction may play a critical role in the microscopic mechanism of the SRC phase’s emergence.

Model and Methods.– The Rydberg atom arrays coupled with cavity-QED can be effectively described by the following Hamiltonian [59, 60]

$$H = \frac{g}{\sqrt{N}} \sum_{i=1}^N (b_i^\dagger a + a^\dagger b_i) + \sum_{\langle i,j \rangle} V_{ij} n_i^{(b)} n_j^{(b)} - \mu n^{(a)} - \mu_b \sum_{i=1}^N n_i^{(b)}, \quad (1)$$

where a denotes the bosonic photon field, b_i is the hardcore bosonic operator describing the Rydberg atom with ground state $|g\rangle$ and excited Rydberg state $|r\rangle$ at the i -th site, and the corresponding density operators are $n^{(a)}$ and $n_i^{(b)}$. The atom-photon coupling strength g can be tuned by adjusting the two-photon process. The chemical potential $\mu < 0$ and gap energy $\Delta = (\mu_b - \mu) > 0$ are related to the photon energy and detuning of the Rydberg atomic energy levels, N is the number of tweezer sites, and the Van der Waals (VdW) interactions between Rydberg states are expressed as $V_{ij} = V/R_{ij}^6$. Here, the VdW interaction is truncated to the nearest neighbor, and the influence of longer interactions will be discussed later.

When the atom-photon coupling is switched off, the Rydberg atoms are decoupled from the cavity, so that the ground state is only governed by the interplay between the VdW interaction and the chemical potential μ_b . At the Z_2 (or spin-up-down) symmetry line $\tilde{\mu} = \mu_b - 3V = 0$, to minimize the ground state energy, one or two atoms are allowed to stay in the Rydberg state inside a triangle unit. Such local constraints can result in macroscopic degeneracy in the ground state [36]. However, a tiny positive (negative) $\tilde{\mu}$ can lift the degeneracy and drive the system away from half-filling so that the translational symmetry is spontaneously broken and the system enters the solid phase with 2/3 (1/3) filling.

In the large g limit, the strong coupling between two-level atoms and the photon can make them form polaritons. Then, their condensation can drive the system into the superradiant (SR) phase, in which the $U(1)$ symmetry is spontaneously broken. According to the Ginzburg-Landau theory, the quantum phase transition between the solid phase and the SR phase should be first order or there exists an intermediate phase between them, such as the superradiant-solid phase which breaks both symmetries just like the SS [59, 60]. Then, it would be interesting to think about the interplay between the quantum photonic field and geometric frustration, both of

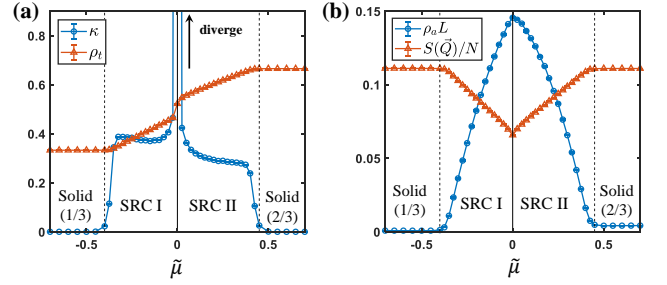


FIG. 2. (a) Compressibility κ and the average total density ρ_t ; (b) photon density ρ_a and the structure factor $S(\vec{Q})/N$, calculated via QMC simulation at $g = 1.8$ and $L = 24$.

which can bring in the disorder.

The QPTs concerning the OBD mechanism are usually unconventional, such as the multi-criticality of the SS phase [18–21], or the deconfined criticality of valence bond crystal [34, 35]. Therefore, it is necessary to borrow high-performance numerical methods. Here, we utilize an efficient large-scale QMC method [59, 60]. The observables are calculated by taking an average of 10^6 samples after half a million thermalization steps, with the inverse temperature set to $\beta = 10L/3$ which is low enough to capture the zero-temperature physics. Without loss of generality, we set $V=1$ as the energy unit and $\Delta = 9$ (the influence of Δ is discussed in the supplementary material (SM) [61]).

Phase Diagram.– In contrast to the classical light field [45], the coupling between the quantized photonic field and two energy levels imposes an additional $U(1)$ symmetry, causing the conservation of the total density $N_t = \langle n^{(a)} + \sum_i n_i^{(b)} \rangle$. Meanwhile, the large energy gap due to the Rydberg interaction makes the trivial solid phases incompressible. Therefore, as shown in Fig. 2 (a), the solid phases can be identified by the plateaus of the average total density $\rho_t = N_t/N$ and zero compressibility $\kappa = N\beta(\langle \rho_t^2 \rangle - \langle \rho_t \rangle^2)$. Certainly, as translational symmetry is spontaneously broken in both the 1/3 and 2/3 solids, they exhibit long-range diagonal correlations, reflected by the nonzero structure factor $S(\vec{Q}) = |s(\vec{Q})|^2$ ($\vec{Q} = (4\pi/3, 0)$) where $s(\vec{Q}) = \langle \sum n_i^{(b)} e^{i\vec{Q}\cdot\vec{R}_i} / \sqrt{N} \rangle$, as shown in Fig. 2 (b). Meanwhile, the energy gap prevents the formation of polaritons, so the photon density $\rho_a = \langle n^{(a)} \rangle/N$ is nearly zero. The slight deviations of ρ_a and $S(\vec{Q})/N$ from their classical limit values 0 and 1/9 can be easily interpreted as second-order perturbations caused by local quantum fluctuations.

Between the two solid phases, the SRC phase can be clearly identified by the nonzero values of both the structure factor and photon density, as shown in Fig. 2(b). The smooth variation of these two order parameters indicates that the phase transition from the SRC phase to the solid phase is of the second order. Analogous to the SS phases in the triangular lattice [19, 20, 62, 63], the emergence of the SRC I (II) phase results from the melting of the 1/3 (2/3) solid phase, triggered by inserting particle (hole) excitations on the honeycomb backbone filled with holes (particles). However, unlike the super-

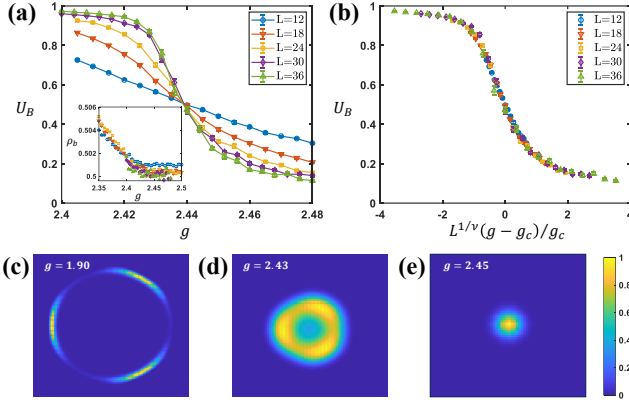


FIG. 3. (a) Binder cumulant U_B at $\tilde{\mu} = 0$ for different system sizes (inset: Rydberg state occupation density), and corresponding (b) finite-size scaling analysis with data collapse. The extracted critical exponent is $1/\nu = 1.50 \pm 0.09$ with phase transition point $g_c = 2.440 \pm 0.00072$. (c-e) Histogram of $s(\vec{Q})$ in the complex plane for different g at $L = 24$.

fluid flowing on the honeycomb backbone in the SS phase, the spontaneous $U(1)$ symmetry breaking in the SRC phase is due to the effective infinite long-range interaction among polaritons teleporting on the honeycomb backbone. We have also calculated the quantum phase boundaries analytically using strong coupling expansion methods [59, 63], and they match very well with the numerical results (see SM [61]). Following this scenario, if we examine the average local magnetization $m = n^{(b)} - 1/2$ in the three sublattices, the corresponding signs in the SRC I and II phases would be $(-, -, +)$ and $(-, +, +)$, respectively (see SM [61]). Given their strong distinction from the $(-, 0, +)$ signature of the OBD phase in the classical light field, the existence of the $(-, 0, +)$ phase along the Z_2 symmetry line becomes highly challenging.

While approaching $\tilde{\mu} = 0$, the number of photons continuously increases, indicating the proliferation of polaritons accompanied by a descent in the structure factors. The finite κ reflects that the SRC phase is compressible, and the divergence of κ with a sudden jump of ρ_t occurring precisely at $\tilde{\mu} = 0$ directly points to an obvious first-order QPT, rather than a possible intermediate $(-, 0, +)$ phase. However, as shown in Fig. 2(b), neither the structure factor nor the photon density exhibits any discontinuities. To detect the QPTs around $\tilde{\mu} = 0$ in more detail, we further consider the dimensionless quantity: the Binder cumulant of the structure factor, $U_B = 2 - \langle S(\vec{Q})^2 \rangle / \langle S(\vec{Q}) \rangle^2$, which equals one in the ordered phase and zero in the disordered phase.

In contrast to frustrated magnetism, at $\tilde{\mu} = 0$ which corresponds to zero longitudinal magnetic fields, the Z_2 symmetry cannot be preserved when coupled to the cavity-QED. Consequently, the Rydberg state occupation density $\rho_b = \langle \sum_i n_i^{(b)} \rangle / N$ is slightly larger than $1/2$ in the SRC phases at small g (see inset of Fig. 3(a)). Meanwhile, as shown in Fig. 3(a), neither the structure factor nor the Binder cumulant exhibits any discontinuity along the variation of g for different system sizes up to $L = 36$. This indicates that the

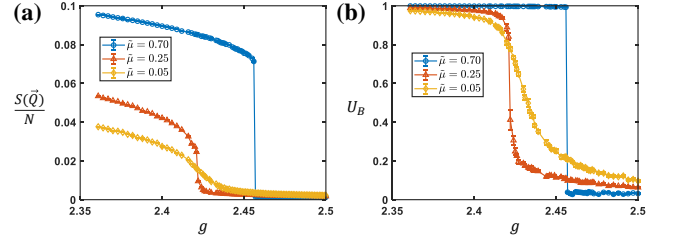


FIG. 4. (a) Structure factor $S(\vec{Q})/N$ and (b) its Binder cumulant U_B calculated by QMC simulation across the SRC-SR transition away from the Z_2 symmetry line for $L = 24$.

QPT from the SRC phase to the SR phase is continuous at $\tilde{\mu} = 0$. To determine the critical exponents, we performed finite-size scaling analysis via the data collapse of the Binder cumulant [34]. As illustrated in Fig. 3(b), after rescaling the atom-photon coupling as $L^{1/\nu}(g/g_c - 1)$, the Binder cumulants for different system sizes collapse into a single curve, with a fitting critical point of $g_c = 2.440 \pm 0.00072$. Additionally, the extracted critical exponent $1/\nu = 1.50 \pm 0.09$ closely matches that of the 3D XY model at the finite-temperature phase transition $\nu = 0.662(7)$ [64]. This suggests that the second-order phase transition from the SRC phase to the SR phase likely belongs to the 3D XY universality class [37, 38, 57, 65].

Similar to the Ginzburg-Landau theory of the XXZ model [20], the stability of the SRC is expected to be determined by the competition between the threefold clock term $M|\psi|^3 \cos(3\theta)$ and the sixfold clock term $|\psi|^6 \cos(6\theta)$, where $\psi = |\psi|e^{i\theta}$ is the order parameter. In the TFIM, the absence of a threefold clock term allows the OBD phase (or clock phase) to emerge. On the other hand, for the XXZ model away from the Z_2 symmetry line, the nonzero uniform magnetization M makes the threefold term relevant, leading to the emergence of the SS phases. However, the nature of the first-order QPT at the Z_2 symmetry line remains debated [57, 58, 65], with a possible tiny spontaneous breaking M potentially causing serious finite-size effects. Fortunately, here M is expected to be modified to $\rho_t - 1/2$ and remains positive at $\tilde{\mu} = 0$ due to the small photon density. Consequently, the system flows into the SRC II phase with a higher $\rho_b > 0.5$. This analysis is supported by the histogram of ψ . At small g (Fig. 3(c)), three clear peaks indicate $(-, +, +)$, confirming the system's presence in the SRC II phase. As the system approaches the critical point (Fig. 3(d)), an irregular circle emerges, hinting at a possible emergent $U(1)$ symmetry (more quantitative discussion shown in SM)[61]. Given that ρ_b attempts to approach $1/2$ when $g \geq g_c$ (see inset of Fig. 3(a)), the revival of Z_2 symmetry might render the threefold clock term irrelevant at the critical point. Considering that the numerical simulation is performed in a finite system, a possible weakly first-order QPT, rather than belonging to the 3D XY universality class, cannot be entirely ruled out in larger system sizes.

Away from the Z_2 symmetry line, the QPT between SRC phases and SR phase changes from continuous to first-order, which is directly reflected by the discontinuity of both the structure factor and the Binder cumulant, as shown in Fig. 4.

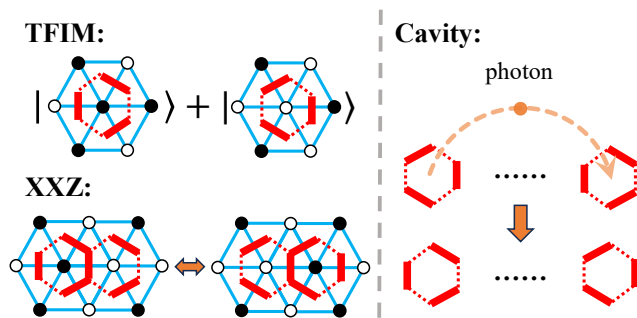


FIG. 5. Dimer representation of ring exchange process in the TFIM, XXZ model, and Rydberg atom array in a cavity.

The first-order QPT begins with two triple points $(\tilde{\mu}, g) \approx (1.00, 2.461)$ and $(-0.95, 2.850)$. As the magnitude of $\tilde{\mu}$ close to the 3D XY point, the discontinuities of the structure factor become systematically smaller. In Fig.4, we can observe that the first-order phase transition terminates at the tri-critical point $(\tilde{\mu}, g) \approx (0.25, 2.421)$ in the case of QPT between SRC II and SR phase under finite system size $L = 24$. However, we still cannot rule out the possibility that the appearance of the tri-critical point [19] is due to the finite size effect, and they may also emerge or merge with the 3D XY critical point in the thermodynamic limit. Discussion about the possible tricriticality can be found in SM [61].

Quantum Dimer Model.— The ground state of frustrated magnetism can typically be described using dimer language. As shown in Fig. 5, bonds with the same states can be mapped to dimers, allowing the Rydberg occupation configuration in the triangular lattice to be mapped to the dimer configuration in the dual honeycomb lattice [37, 38]. Consequently, the local constraint in each triangle is transferred to a single dimer linking to the dual site, and all possible degenerate ground states can be classified into different topological sectors based on winding numbers [24] (More discussions in SM [61]). Compared to the solid phase, the disordered state with high degeneracy at half-filling is expected to be unstable under the perturbation of atom-photon coupling. Considering an atom in the Rydberg state surrounded by an alternatively occupied hexagon depicted as , it can return to the state  and emit a photon without violating the local constraint. In dimer language, this corresponds to the ring ex-

change in the hexagon . Meanwhile, as demonstrated in Fig. 5, another ring exchange can occur by absorbing a photon from a distant location. Thus, the cavity-mediated long-range ring exchange between two hexagons is nonlocal, similar to the double-hexagon ring-exchange process in the XXZ model [56]. We can argue that such nonlocal ring exchange may significantly lower the energy of the SRC phase, akin to the effect of XY interactions [58].

Conclusion and Discussion.— Our QMC simulations of Rydberg atomic triangular arrays coupled with cavity-QED reveal the emergence of novel SRC phases and rich QPT phenomena, driven by the competition between sixfold and threefold clock terms. In real experiments, Rydberg atom interactions extend beyond nearest neighbors, but both experimental [45] and numerical [66] studies indicate that long-range interactions only slightly alter the OBD phase region which is also discussed in SM [61]. Certainly, the impact of long-range interactions on SRC phases, particularly their interplay with emergent U(1) lattice gauge theory [24, 25], warrants further investigation. Especially, the recent advance of the Rydberg dressing atom in the optical lattice could make the system to be more larger and meanwhile get rid of the long-range interaction tail’s influence [67].

Our simulations assume a perfect, non-leaking cavity. However, cavity imperfections in real experiments could significantly affect the OBD mechanism, the influences of the cavity leakage and inhomogeneity are discussed in SM [61]. Other frustrated geometries coupled with cavity-QED, such as the Kagome lattice [49, 68] and spin ice [69], may also present intriguing possibilities for disorder-by-disorder phenomena and emergent QED physics. In summary, we believe that cavity-mediated infinite long-range interactions can profoundly alter our understanding of emergent physics in both frustrated systems and many-body quantum optics.

ACKNOWLEDGMENTS

We would like to thank Changle Liu for many helpful discussions and especially for sharing the data of Ref.[40]. X.-F. Z. acknowledges funding from the National Science Foundation of China under Grants No.12274046 and No.12547101, and Xiaomi Foundation / Xiaomi Young Talents Program.

- [1] P. Forn-Díaz, L. Lamata, E. Rico, J. Kono, and E. Solano, “Ultrastrong coupling regimes of light-matter interaction,” *Rev. Mod. Phys.* **91**, 025005 (2019).
- [2] Nicolò Defenu, Tobias Donner, Tommaso Macrì, Guido Pagano, Stefano Ruffo, and Andrea Trombettoni, “Long-range interacting quantum systems,” *Rev. Mod. Phys.* **95**, 035002 (2023).
- [3] D. Braak, “Integrability of the rabi model,” *Phys. Rev. Lett.* **107**, 100401 (2011).

- [4] Myung-Joong Hwang, Ricardo Puebla, and Martin B. Plenio, “Quantum phase transition and universal dynamics in the rabi model,” *Phys. Rev. Lett.* **115**, 180404 (2015).
- [5] Maoxin Liu, Stefano Chesi, Zu-Jian Ying, Xiaosong Chen, Hong-Gang Luo, and Hai-Qing Lin, “Universal scaling and critical exponents of the anisotropic quantum rabi model,” *Phys. Rev. Lett.* **119**, 220601 (2017).
- [6] Han-Jie Zhu, Kai Xu, Guo-Feng Zhang, and Wu-Ming Liu, “Finite-component multicriticality at the superradiant quantum phase transition,” *Phys. Rev. Lett.* **125**, 050402 (2020).

- [7] Guitao Lyu, Korbinian Kottmann, Martin B. Plenio, and Myung-Joong Hwang, “Multicritical dissipative phase transitions in the anisotropic open quantum rabi model,” *Phys. Rev. Res.* **6**, 033075 (2024).
- [8] Yu-Yu Zhang, Zi-Xiang Hu, Libin Fu, Hong-Gang Luo, Han Pu, and Xue-Feng Zhang, “Quantum phases in a quantum rabi triangle,” *Phys. Rev. Lett.* **127**, 063602 (2021).
- [9] Jinchun Zhao and Myung-Joong Hwang, “Frustrated superradiant phase transition,” *Phys. Rev. Lett.* **128**, 163601 (2022).
- [10] Diego Fallas Padilla, Han Pu, Guo-Jing Cheng, and Yu-Yu Zhang, “Understanding the quantum rabi ring using analogies to quantum magnetism,” *Phys. Rev. Lett.* **129**, 183602 (2022).
- [11] Brendan P. Marsh, Ronen M. Kroeze, Surya Ganguli, Sarang Gopalakrishnan, Jonathan Keeling, and Benjamin L. Lev, “Entanglement and replica symmetry breaking in a driven-dissipative quantum spin glass,” *Phys. Rev. X* **14**, 011026 (2024).
- [12] Tharnier O. Puel and Tommaso Macrì, “Confined meson excitations in rydberg-atom arrays coupled to a cavity field,” *Phys. Rev. Lett.* **133**, 106901 (2024).
- [13] Jonas Rohn, Max Hörmann, Claudiu Genes, and Kai Phillip Schmidt, “Ising model in a light-induced quantized transverse field,” *Phys. Rev. Res.* **2**, 023131 (2020).
- [14] Zeno Bacciconi, Hernan B. Xavier, Matteo Marinelli, Deendra Singh Bhakuni, and Marcello Dalmonte, “Meson-polariton and string dynamics via cavity coupling in rydberg atom array,” (2025), arXiv:2501.04634 [quant-ph].
- [15] Aleksandr N. Mikheev, Hossein Hosseinabadi, and Jamir Marino, “Prethermalization of Light and Matter in Cavity-Coupled Rydberg Arrays,” *Phys. Rev. Lett.* **135**, 210402 (2025), arXiv:2504.06267 [cond-mat.stat-mech].
- [16] Charlie-Ray Mann, Mark A. Oehlgrien, Błażej Jaworowski, Giuseppe Calajó, Jamir Marino, Kyung S. Choi, and Darriek E. Chang, “Squeezing classical antiferromagnets into quantum spin liquids via global cavity fluctuations,” (2025), arXiv:2512.05630 [quant-ph].
- [17] Robert Mattes, Igor Lesanovsky, and Federico Carollo, “Long-range interacting systems are locally noninteracting,” *Phys. Rev. Lett.* **134**, 070402 (2025).
- [18] Daisuke Yamamoto, Giacomo Marmorini, and Ipeei Danshita, “Quantum Phase Diagram of the Triangular-Lattice XXZ Model in a Magnetic Field,” *Phys. Rev. Lett.* **112**, 127203 (2014), arXiv:1309.0086 [cond-mat.str-el].
- [19] Daniel Sellmann, Xue-Feng Zhang, and Sebastian Eggert, “Phase diagram of the antiferromagnetic XXZ model on the triangular lattice,” *Phys. Rev. B* **91**, 081104 (2015), arXiv:1403.0008 [cond-mat.str-el].
- [20] R. G. Melko, A. Paramekanti, A. A. Burkov, A. Vishwanath, D. N. Sheng, and L. Balents, “Supersolid Order from Disorder: Hard-Core Bosons on the Triangular Lattice,” *Phys. Rev. Lett.* **95**, 127207 (2005), arXiv:cond-mat/0505258 [cond-mat.str-el].
- [21] Junsen Xiang, Chuandi Zhang, Yuan Gao, Wolfgang Schmidt, Karin Schmalzl, Chin-Wei Wang, Bo Li, Ning Xi, Xinyang Liu, Hai Jin, Gang Li, Jun Shen, Ziyu Chen, Yang Qi, Yuan Wan, Wentao Jin, Wei Li, Peijie Sun, and Gang Su, “Giant magnetocaloric effect in spin supersolid candidate $\text{Na}_2\text{BaCo}(\text{PO}_4)_2$,” *Nature (London)* **625**, 270–275 (2024).
- [22] John B. Kogut, “An introduction to lattice gauge theory and spin systems,” *Rev. Mod. Phys.* **51**, 659–713 (1979).
- [23] Rhine Samajdar, Darshan G. Joshi, Yanting Teng, and Subir Sachdev, “Emergent \mathbb{Z}_2 Gauge Theories and Topological Excitations in Rydberg Atom Arrays,” *Phys. Rev. Lett.* **130**, 043601 (2023), arXiv:2204.00632 [cond-mat.quant-gas].
- [24] Zheng Zhou, Zheng Yan, Changle Liu, Yan Chen, and Xue-Feng Zhang, “Quantum Simulation of Two-Dimensional U(1) Gauge Theory in Rydberg and Rydberg-Dressed Atom Arrays,” *Chinese Physics Letters* **42**, 053705 (2025), arXiv:2212.10863 [quant-ph].
- [25] Zheng Yan, Zheng Zhou, Yan-Hua Zhou, Yan-Cheng Wang, Xingze Qiu, Zi Yang Meng, and Xue-Feng Zhang, “Quantum optimization within lattice gauge theory model on a quantum simulator,” *npj Quantum Information* **9**, 89 (2023), arXiv:2105.07134 [quant-ph].
- [26] Yi Zhou, Kazushi Kanoda, and Tai-Kai Ng, “Quantum spin liquid states,” *Rev. Mod. Phys.* **89**, 025003 (2017).
- [27] Leon Balents, “Spin liquids in frustrated magnets,” *Nature* **464**, 199–208 (2010).
- [28] C. Broholm, R. J. Cava, S. A. Kivelson, D. G. Nocera, M. R. Norman, and T. Senthil, “Quantum spin liquids,” *Science* **367**, eaay0668 (2020), <https://www.science.org/doi/pdf/10.1126/science.aay0668>.
- [29] T. Senthil, Ashvin Vishwanath, Leon Balents, Subir Sachdev, and Matthew P. A. Fisher, “Deconfined quantum critical points,” *Science* **303**, 1490 (2004).
- [30] Kun Chen, Yuan Huang, Youjin Deng, A. B. Kuklov, N. V. Prokof'ev, and B. V. Svistunov, “Deconfined criticality flow in the heisenberg model with ring-exchange interactions,” *Phys. Rev. Lett.* **110**, 185701 (2013).
- [31] Anders W. Sandvik, “Evidence for deconfined quantum criticality in a two-dimensional heisenberg model with four-spin interactions,” *Phys. Rev. Lett.* **98**, 227202 (2007).
- [32] Yi Cui, Lu Liu, Huihang Lin, Kai-Hsin Wu, Wenshan Hong, Xuefei Liu, Cong Li, Ze Hu, Ning Xi, Shiliang Li, Rong Yu, Anders W. Sandvik, and Weiqiang Yu, “Proximate deconfined quantum critical point in $\text{SrCu}_2(\text{BO}_3)_2$,” *Science* **380**, 1179–1184 (2023), arXiv:2204.08133 [cond-mat.str-el].
- [33] Yan Qi Qin, Yuan-Yao He, Yi-Zhuang You, Zhong-Yi Lu, Arnab Sen, Anders W. Sandvik, Cenke Xu, and Zi Yang Meng, “Duality between the deconfined quantum-critical point and the bosonic topological transition,” *Phys. Rev. X* **7**, 031052 (2017).
- [34] Xue-Feng Zhang, Yin-Chen He, Sebastian Eggert, Roderich Moessner, and Frank Pollmann, “Continuous easy-plane deconfined phase transition on the kagome lattice,” *Phys. Rev. Lett.* **120**, 115702 (2018).
- [35] Dong-Xu Liu, Zijian Xiong, Yining Xu, and Xue-Feng Zhang, “Deconfined quantum phase transition on the kagome lattice: Distinct velocities of spinon and string excitations,” *Phys. Rev. B* **109**, L140404 (2024), arXiv:2301.12864 [cond-mat.str-el].
- [36] G. H. Wannier, “Antiferromagnetism. the triangular ising net,” *Physical Review* **79**, 357–364 (1950).
- [37] R. Moessner, S. L. Sondhi, and P. Chandra, “Two-Dimensional Periodic Frustrated Ising Models in a Transverse Field,” *Phys. Rev. Lett.* **84**, 4457–4460 (2000), arXiv:cond-mat/9910499 [cond-mat.stat-mech].
- [38] R. Moessner, S. L. Sondhi, and P. Chandra, “Phase diagram of the hexagonal lattice quantum dimer model,” *Phys. Rev. B* **64**, 144416 (2001).
- [39] P. Fazekas and P. W. Anderson, “On the ground state properties of the anisotropic triangular antiferromagnet,” *Philosophical Magazine* **30**, 423–440 (1974).
- [40] Changle Liu, Chun-Jiong Huang, and Gang Chen, “Intrinsic quantum ising model on a triangular lattice magnet tm mg ga o_4 ,” *Physical Review Research* **2**, 043013 (2020).
- [41] Antoine Browaeys and Thierry Lahaye, “Many-body physics with individually controlled rydberg atoms,” *Nat. Phys.* **16**, 132–142 (2020).

- [42] Bao-Yun Dong, Yanhua Zhou, Wei Wang, and Tao Wang, “Engineering an anisotropic dicker model of rydberg atom arrays in an optical cavity with dipole–dipole interactions,” *Chinese Physics B* **34** (2025).
- [43] Hannes Bernien, Sylvain Schwartz, Alexander Keesling, Harry Levine, Ahmed Omran, Hannes Pichler, Soonwon Choi, Alexander S. Zibrov, Manuel Endres, Markus Greiner, Vladan Vuletić, and Mikhail D. Lukin, “Probing many-body dynamics on a 51-atom quantum simulator,” *Nature (London)* **551**, 579–584 (2017), arXiv:1707.04344 [quant-ph].
- [44] Sepehr Ebadi, Tout T. Wang, Harry Levine, Alexander Keesling, Giulia Semeghini, Ahmed Omran, Dolev Bluvstein, Rhine Samajdar, Hannes Pichler, Wen Wei Ho, Soonwon Choi, Subir Sachdev, Markus Greiner, Vladan Vuletić, and Mikhail D. Lukin, “Quantum phases of matter on a 256-atom programmable quantum simulator,” *Nature (London)* **595**, 227–232 (2021), arXiv:2012.12281 [quant-ph].
- [45] Pascal Scholl, Michael Schuler, Hannah J. Williams, Alexander A. Eberharter, Daniel Barredo, Kai-Niklas Schymik, Vincent Lienhard, Louis-Paul Henry, Thomas C. Lang, Thierry Lahaye, Andreas M. Läuchli, and Antoine Browaeys, “Quantum simulation of 2D antiferromagnets with hundreds of Rydberg atoms,” *Nature (London)* **595**, 233–238 (2021), arXiv:2012.12268 [quant-ph].
- [46] G. Semeghini, H. Levine, A. Keesling, S. Ebadi, T. T. Wang, D. Bluvstein, R. Verresen, H. Pichler, M. Kalinowski, R. Samajdar, A. Omran, S. Sachdev, A. Vishwanath, M. Greiner, V. Vuletić, and M. D. Lukin, “Probing topological spin liquids on a programmable quantum simulator,” *Science* **374**, 1242–1247 (2021), arXiv:2104.04119 [quant-ph].
- [47] Rhine Samajdar, Wen Wei Ho, Hannes Pichler, Mikhail D. Lukin, and Subir Sachdev, “Quantum phases of Rydberg atoms on a kagome lattice,” *Proceedings of the National Academy of Science* **118**, e2015785118 (2021), arXiv:2011.12295 [cond-mat.quant-gas].
- [48] Zheng Yan, Yan-Cheng Wang, Rhine Samajdar, Subir Sachdev, and Zi Yang Meng, “Emergent Glassy Behavior in a Kagome Rydberg Atom Array,” *Phys. Rev. Lett.* **130**, 206501 (2023), arXiv:2301.07127 [cond-mat.quant-gas].
- [49] Daniel González-Cuadra, Majd Hamdan, Torsten V. Zache, Boris Braverman, Milan Kornjača, Alexander Lukin, Sergio H. Cantú, Fangli Liu, Sheng-Tao Wang, Alexander Keesling, Mikhail D. Lukin, Peter Zoller, and Alexei Bylinskii, “Observation of string breaking on a $(2 + 1)$ D Rydberg quantum simulator,” *Nature (London)* **642**, 321–326 (2025), arXiv:2410.16558 [quant-ph].
- [50] Wei Xu and Xue-Feng Zhang, “Geometric breaking of quantum strings in kagome rydberg atom array,” (2025), arXiv:2410.21135 [cond-mat.quant-gas].
- [51] Emma Deist, Justin A. Gerber, Yue-Hui Lu, Johannes Zeiher, and Dan M. Stamper-Kurn, “Superresolution microscopy of optical fields using tweezer-trapped single atoms,” *Phys. Rev. Lett.* **128**, 083201 (2022).
- [52] Zhenjie Yan, Jacquelyn Ho, Yue-Hui Lu, Stuart J. Masson, Ana Asenjo-Garcia, and Dan M. Stamper-Kurn, “Superradiant and subradiant cavity scattering by atom arrays,” *Phys. Rev. Lett.* **131**, 253603 (2023).
- [53] Yanxin Liu, Zhihui Wang, Pengfei Yang, Qinxia Wang, Qing Fan, Shijun Guan, Gang Li, Pengfei Zhang, and Tiancai Zhang, “Realization of strong coupling between deterministic single-atom arrays and a high-finesse miniature optical cavity,” *Phys. Rev. Lett.* **130**, 173601 (2023).
- [54] Xiaotian Zhang, Zhanhai Yu, Hongrui Zhang, Di Xiang, and Hao Zhang, “Cavity dark mode mediated by atom array without atomic scattering loss,” *Phys. Rev. Res.* **6**, L042026 (2024).
- [55] Stefan Wessel and Matthias Troyer, “Supersolid hard-core bosons on the triangular lattice,” *Phys. Rev. Lett.* **95**, 127205 (2005).
- [56] Dariush Heidarian and Kedar Damle, “Persistent supersolid phase of hard-core bosons on the triangular lattice,” *Phys. Rev. Lett.* **95**, 127206 (2005).
- [57] Massimo Boninsegni and Nikolay Prokof’ev, “Supersolid phase of hard-core bosons on a triangular lattice,” *Phys. Rev. Lett.* **95**, 237204 (2005).
- [58] Arnab Sen, Prasenjit Dutt, Kedar Damle, and R. Moessner, “Variational wave-function study of the triangular lattice supersolid,” *Phys. Rev. Lett.* **100**, 147204 (2008).
- [59] Xue-Feng Zhang, Qing Sun, Yu-Chuan Wen, Wu-Ming Liu, Sebastian Eggert, and An-Chun Ji, “Rydberg polaritons in a cavity: A superradiant solid,” *Phys. Rev. Lett.* **110**, 090402 (2013).
- [60] Gao-Qi An, Yan-Hua Zhou, Tao Wang, and Xue-Feng Zhang, “Quantum phase transition of a two-dimensional rydberg atom array in an optical cavity,” *Phys. Rev. B* **106**, 134506 (2022).
- [61] See Supplemental Material for a further discussion on the variational approach, strong coupling expansion, influence of the detuning, long-range interaction, cavity leaking, tri-critical points, anisotropy parameter, inhomogeneous effect, superradiant solid phase, and topological sector, which includes Refs. [1–14, 17–41, 43–60, 62–67, 69–77].
- [62] Xue-Feng Zhang, Yu-Chuan Wen, and Sebastian Eggert, “Static impurities in a supersolid of interacting hard-core bosons on a triangular lattice,” *Phys. Rev. B* **82**, 220501 (2010).
- [63] Xue-Feng Zhang, Raoul Dillenschneider, Yue Yu, and Sebastian Eggert, “Supersolid phase transitions for hard-core bosons on a triangular lattice,” *Phys. Rev. B* **84**, 174515 (2011).
- [64] A. P. Gottlob and M. Hasenbusch, “Critical behaviour of the 3d xy-model: A monte carlo study,” *Physica A: Statistical Mechanics and its Applications* **201**, 593–613 (1993), arXiv:cond-mat/9305020.
- [65] Lars Bonnes and Stefan Wessel, “Generic first-order versus continuous quantum nucleation of supersolidity,” *Phys. Rev. B* **84**, 054510 (2011).
- [66] Sibao Guo, Juntao Huang, Jiangping Hu, and Zi-Xiang Li, “Order by disorder and an emergent kosterlitz-thouless phase in a triangular rydberg array,” *Phys. Rev. A* **108**, 053314 (2023).
- [67] Pascal Weckesser, Kritsana Srakaew, Tizian Blatz, David Wei, Daniel Adler, Suchita Agrawal, Annabelle Bohrdt, Immanuel Bloch, and Johannes Zeiher, “Realization of a rydberg-dressed extended bose-hubbard model,” *Science* **390**, 849–853 (2025), <https://www.science.org/doi/pdf/10.1126/science.adq7082>.
- [68] Chenan Wei, Liu Yang, and Qing-Dong Jiang, “Cavity-vacuum-induced chiral spin liquids in kagome lattices: Tuning and probing topological quantum phases via cavity quantum electrodynamics,” *Phys. Rev. Lett.* **135**, 236901 (2025).
- [69] Jeet Shah, Gautam Nambiar, Alexey V. Gorshkov, and Victor Galitski, “Quantum spin ice in three-dimensional rydberg atom arrays,” *Phys. Rev. X* **15**, 011025 (2025).
- [70] Neill Lambert, Eric Giguère, Paul Mencil, Boxi Li, Patrick Hopf, Gerardo Suarez, Marc Gali, Jake Lishman, Rushiraj Gadhvi, Rochisha Agarwal, Asier Galicia, Nathan Shammah, Paul Nation, J. R. Johansson, Shahnawaz Ahmed, Simon Cross, Alexander Pitchford, and Franco Nori, “Qutip 5: The quantum toolbox in Python,” *Physics Reports* **1153**, 1–62 (2026).
- [71] Jérôme Houdayer and Alexander Hartmann, “Low-temperature behavior of two-dimensional gaussian ising spin glasses,” *Phys. Rev. B* **70**, 014418 (2004).
- [72] Lucile Savary and Leon Balents, “Quantum spin liquids: A review,” *Reports on Progress in Physics* **80** (2016), 10.1088/0034-

4885/80/1/016502.

- [73] Yanxin Liu, Zhihui Wang, Pengfei Yang, Qinxia Wang, Qing Fan, Shijun Guan, Gang Li, Pengfei Zhang, and Tiancai Zhang, “Realization of strong coupling between deterministic single-atom arrays and a high-finesse miniature optical cavity,” *Phys. Rev. Lett.* **130**, 173601 (2023).
- [74] Zheng Zhou, Changle Liu, Dong-Xu Liu, Zheng Yan, Yan Chen, and Xue-Feng Zhang, “Quantum tricriticality of incommensurate phase induced by quantum strings in frustrated Ising magnetism,” *SciPost Phys.* **14**, 037 (2023).
- [75] Xiaotian Zhang, Zhanhai Yu, Hongrui Zhang, Di Xiang, and Hao Zhang, “Cavity dark mode mediated by atom array without atomic scattering loss,” *Phys. Rev. Res.* **6**, L042026 (2024).
- [76] Xue-Feng Zhang, Shijie Hu, Axel Pelster, and Sebastian Eggert, “Quantum domain walls induce incommensurate supersolid phase on the anisotropic triangular lattice,” *Phys. Rev. Lett.* **117**, 193201 (2016).
- [77] Zheng Yan, Zheng Zhou, Yan-Hua Zhou, Yan-Cheng Wang, Xingze Qiu, Zi Yang Meng, and Xue-Feng Zhang, “Quantum optimization within lattice gauge theory model on a quantum simulator,” *npj Quantum Information* **9**, 89 (2023).
- [78] Gao-Qi An, Yan-Hua Zhou, Tao Wang, and Xue-Feng Zhang, “Quantum phase transition of a two-dimensional rydberg atom array in an optical cavity,” *Phys. Rev. B* **106**, 134506 (2022).

I. SUPPLEMENTAL MATERIAL

A. Variational Approach

The ground state phase diagram can also be calculated by using the variational approach, and the corresponding variational wave function can be explicitly written as

$$|\lambda, \theta_i\rangle = e^{-\frac{\lambda\sqrt{N}}{2}a^\dagger} \otimes \prod_i \left[\cos\left(\frac{\theta_i}{2}\right)b_i^\dagger + \sin\left(\frac{\theta_i}{2}\right) \right] |0\rangle, \quad (2)$$

where $i = A, B, C$ labels the three sublattices, λ , and θ_i are the variational parameters for the quantum photonic field and Rydberg atom states. Then, the variational energy per site can be calculated and equals

$$\begin{aligned} E &= \frac{\langle \lambda, \theta | H | \lambda, \theta \rangle}{N} \\ &= -\frac{g\lambda}{6} (\sin \theta_A + \sin \theta_B + \sin \theta_C) - \frac{\lambda^2 \mu}{4} \\ &\quad - \frac{1}{6} (\cos \theta_A + \cos \theta_B + \cos \theta_C + 3) (\mu + \Delta) \\ &\quad + \frac{V}{4} (\cos \theta_A \cos \theta_B + \cos \theta_B \cos \theta_C + \cos \theta_C \cos \theta_A \\ &\quad + 2 \cos \theta_A + 2 \cos \theta_B + 2 \cos \theta_C + 3). \end{aligned} \quad (3)$$

From the expression, we find out that the region of the variational parameters can be limited to $\lambda \geq 0$ and $0 \leq \theta_A \leq \theta_B \leq \theta_C \leq \pi$ so that the minimisation of the variational energy can be simplified. The different phases can be characterised by the variational values listed in Table I.

The variational phase diagram is shown in Fig.6, and we can find an intermediate phase between SRC phases instead of the first-order QPT. To check its structure, we calculate

Parameters	SRC I	SRC II	SRC 0	solid(1/3)	solid(2/3)	SR
λ	$\neq 0$	$\neq 0$	$\neq 0$	0	0	$\neq 0$
θ_A	$\theta_1 < \frac{\pi}{2}$	$\theta_1 < \frac{\pi}{2}$	θ_1	0	0	θ
θ_B	$\theta_3 > \frac{\pi}{2}$	$\theta_1 < \frac{\pi}{2}$	θ_2	0	π	θ
θ_C	$\theta_3 > \frac{\pi}{2}$	$\theta_3 > \frac{\pi}{2}$	θ_3	π	π	θ

TABLE I. The variational values for different phases, where $\theta_1 < \theta_2 < \theta_3$ in SRC 0 phase. These values are determined by minimizing Eq.(3).

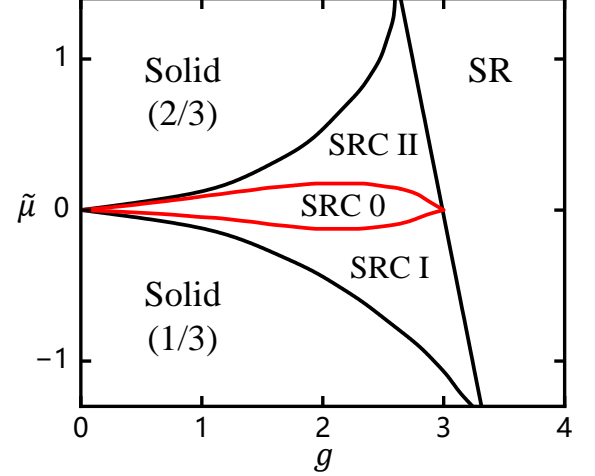


FIG. 6. Variational phase diagram for $\Delta = 9$ and $V = 1$.

the Rydberg state occupation density of the three sublattices $\rho_b^i = \cos^2(\theta_i/2)$, which are plotted in Fig.7. Surprisingly, at Z_2 symmetry point, the local magnetisation presents $(+, 0, -)$ structure which is the same as the OBD phase. Considering its photon density is nonzero, we name it as SRC 0 phase. The $(+, 0, -)$ structure indicates the SRC 0 phase is driven by the sixfold clock term. In the variational approach, the quantum photon field is replaced with a coherent state of light, which is the most classical state of light, so the quantum property of the light is heavily underestimated. Therefore, by comparing with the quantum phase diagram via the QMC method in Fig.1 in the main text, we think the SRC I and II phases can gain more energy from quantum fluctuations so that the OBD phase (or SRC 0 phase) is totally suppressed. Furthermore, in the real experiment, the leaking of the cavity makes the light behave more “classical”, so the intermediate SRC 0 phase may emerge in the frustrated open system coupled with the cavity.

B. Strong Coupling Expansion Method

The phase transition from the solid phases to the SRC phases is continuous and induced by exciting the polariton on the honeycomb lattice backbone. Considering the QPT happens at a small g , it is possible to utilize the strong coupling expansion (SCE) method by taking the atom-light coupling interaction as a perturbative term.

Therefore, the corresponding critical lines can be calcu-

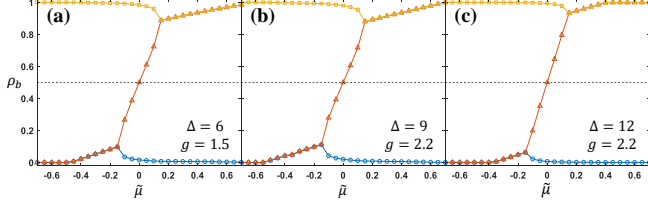


FIG. 7. Variational results of the Rydberg state occupation density in three sublattices under different detuning.

lated. For the phase transition from solid (1/3) to SRC I phase, we can calculate the second-order perturbation energy of the solid (1/3) phase as $E_{1/3} = -N(\tilde{\mu}/3 + V) + g^2/3\Delta$. When entering the SRC I phase, we consider excitation of a Rydberg state based on the 1/3-filled background and obtain the second-order perturbation energy: $E'_{1/3} = -(\tilde{\mu} + 3V)(N/3 - 1) + 3V - 2g^2/(3\Delta - 9V) - g^2/3\Delta$. At the phase boundary, $E_{1/3}$ and $E'_{1/3}$ should be equal, so we can determine the phase boundary:

$$\tilde{\mu}_{c1} = -\frac{2g^2}{3(\Delta - 3V)}. \quad (4)$$

Similarly, for the phase transition from the solid (2/3) phase to the SRC II phase, the second-order perturbation energies are: $E_{2/3} = -2N(\tilde{\mu}/3 + V) + NV + 2g^2/(3\Delta - 9V)$ and $E'_{2/3} = -(\tilde{\mu} + 3V)(2N/3 - 1) + (N - 3)V - 4g^2/(3\Delta - 9V)$, which correspond to the 2/3-filled state and its hole excitation. Thus, we can determine the phase boundary

$$\tilde{\mu}_{c2} = \frac{2g^2}{3(\Delta - 3V)}. \quad (5)$$

As demonstrated in Fig.8, the phase boundary given by SCE is close to the QMC results, especially the lower critical line $\tilde{\mu}_{c1}$. From Fig.2 (b) in the main text, we can find that the photon density around the upper critical line $\tilde{\mu}_{c2}$ is larger than $\tilde{\mu}_{c1}$, so the large deviation of the upper critical line may result from the high order perturbation's non-negligible contribution.

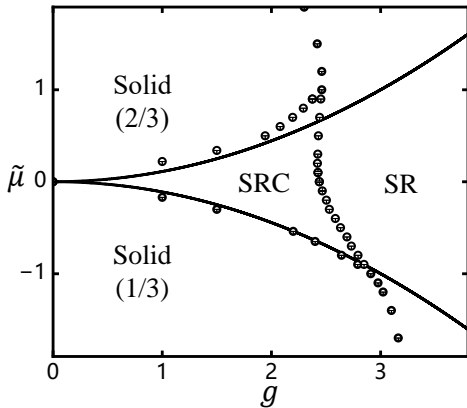


FIG. 8. Phase boundaries determined by SCE (solid line) and QMC (circle) with same parameters as Fig.1 in the main text.

C. Influence of the Detuning

The experiment in the canonical ensemble can be transformed to the following Hamiltonian in the grand canonical ensemble [60]:

$$H = \frac{g}{\sqrt{N}} \sum_{i=1}^N (b_i^\dagger a + a^\dagger b_i) + \sum_{\langle ij \rangle} V_{ij} n_i^{(b)} n_j^{(b)} + \omega_c n^{(a)} + \epsilon \sum_{i=1}^N n_i^{(b)} - \mu_t N_t, \quad (6)$$

where ω_c and ϵ are the cavity and atom transition frequencies with the detuning defined by $\Delta = \omega_c - \epsilon$. Then, after comparing with Eq.(1) in the main text, we can immediately find out $\mu = \mu_t - \omega_c$ and $\mu_b = \mu_t - \epsilon = \mu_t - (\omega_c - \Delta) = \mu + \Delta$. Meanwhile, to reflect the Z_2 (or spin-up-down) symmetry, we introduce $\tilde{\mu} = \mu_b - 3V$, so we can get the relation $\mu = \tilde{\mu} + 3V - \Delta$. In the numerical simulation, the values of $V = 1$ and $\Delta = 9$ are fixed, so the $\tilde{\mu} - g$ phase diagram can be directly transformed to the $\mu - g$ phase diagram. Therefore, although μ is related to the frequency of the photon ω_c , adjusting ω_c and ϵ in the experiment is equivalent to tuning the value of Δ . Then, it would be necessary to discuss the influence of the detuning.

According to the Ginzburg-Landau theory discussed in the main text, the photon number density of the system is likely to influence the energy gap of the first-order phase transition. To ensure that the first-order phase transition shown in Fig. 2 in the main text remains stable under different detunings, we calculated the compressibility κ and the total particle number density ρ_t for different detunings. The results presented in Fig. 9(a,b) demonstrate that the signal of the first-order phase transition remains robust under different detunings.

We can also examine the Rydberg state occupation density in three sublattices at different detunings. As demonstrated in Fig. 9(c,d), the local magnetization in the SRC I and II phases

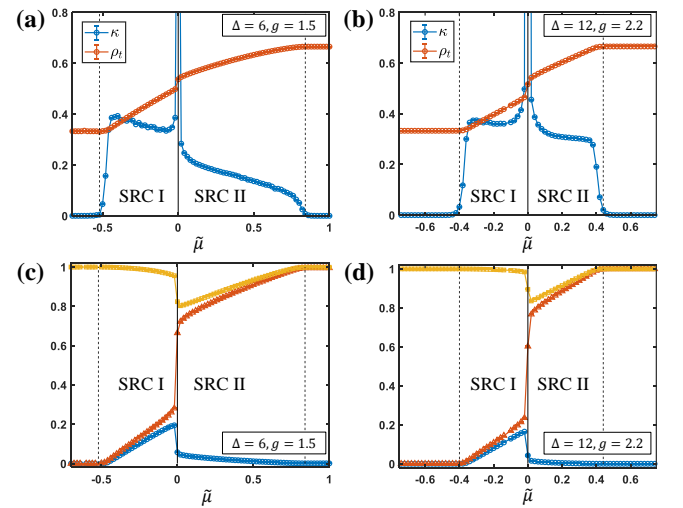


FIG. 9. (a,b) Compressibility κ , the average total density ρ_t , and (c,d) Rydberg state occupation density in three sublattices calculated by QMC simulation at $L = 24$ with different detuning.

shows a clear feature of sign structure $(-, -, +)$ and $(-, +, +)$, respectively. Compared to the variational results, the densities at the backbone two sublattices are different. This discrepancy may be attributed to the possible SRC 0 phase due to the finite temperature effects.

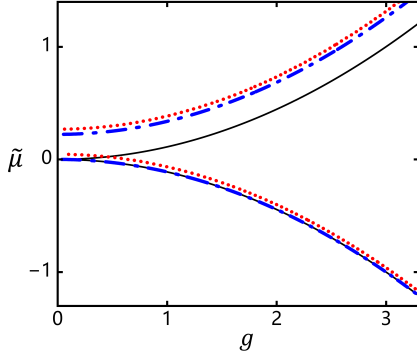


FIG. 10. Phase boundaries between SRC and solid phase, determined by the SCE with $\Delta = 9$ and Rydberg repulsive interaction truncated up to nearest-neighbor (black solid line), next nearest-neighbor (blue dot dashed line), and next next nearest-neighbor sites (red dotted line).

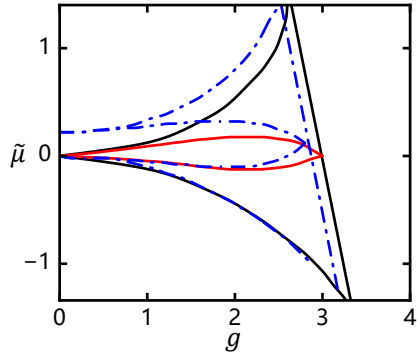


FIG. 11. Phase diagram calculated via variational approach at $\Delta = 9$. The blue dot dashed line takes into account the NN interaction, in comparison with the solid lines shown in Fig. 6.

D. long-range interaction

Since the VdW interaction between Rydberg atoms is actually a long-range interaction that decays with r^{-6} , in this section, we discuss the effect of further truncation distances on the phase diagram. In the main text, we only consider the nearest neighbor interaction, but here we extend it to the 3rd nearest neighbor interaction with the Hamiltonian below:

$$H = \frac{g}{\sqrt{N}} \sum_{i=1}^N (b_i^\dagger a + a^\dagger b_i) + \sum_{k=0}^2 \sum_{ij}^N V_k n_i^{(b)} n_j^{(b)} - \mu n^{(a)} - \mu_b \sum_{i=1}^N n_i^{(b)}, \quad (7)$$

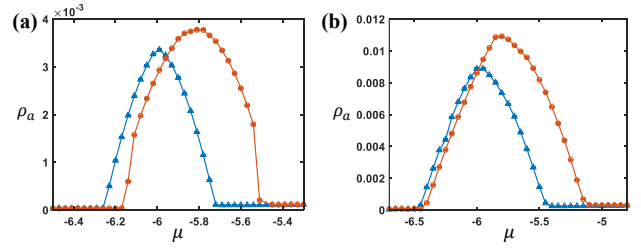


FIG. 12. The photon density ρ_a vs chemical potential μ calculated by QMC simulation at (a) $g = 1.50$ and (b) $g = 2.00$ with $\Delta = 9$, $L = 24$, and the Rydberg repulsive interaction truncated up to nearest-neighbor (blue triangle) and 3rd nearest-neighbor sites (red circle).

where $V_0 = 1$, $V_1 = 1/27$, $V_2 = 1/64$ corresponding to the nearest neighbor(N), next nearest neighbor(NN) and 3rd nearest neighbor(NNN) interactions. With the help of the SCE, we can obtain the analytic expression of the phase boundaries between SRC and solid phases, which are presented in Table II. As shown in Fig. 10, the long-range interaction can only impose a tiny shift. Meanwhile, the results of the variational method (Fig. 11) indicate that the long-range interactions that decay with r^{-6} do not destroy any phases, but only slightly deform the whole phase diagram.

The shift of the phase boundaries can be verified by the simulation of QMC, and is clearly reflected in both Fig. 12 and Fig. 13. Meanwhile, along the Z_2 symmetry line (Fig. 13), we can still observe that the Rydberg atom density $\rho_b > 0.5$, indicating that the ground state is still governed by the $M|\psi|^3 \cos(3\theta)$ term. However, maybe due to the possible glassiness effect introduced by the long-range interaction, it becomes easier to destroy the crystal order, and the critical value g_c decreases to be smaller.

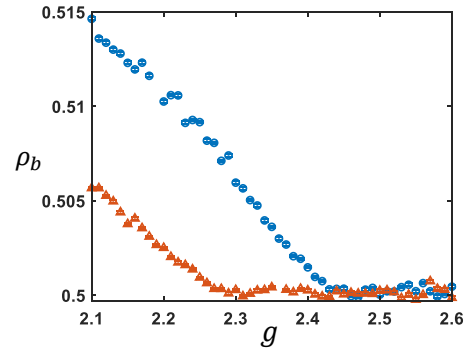


FIG. 13. The Rydberg density ρ_b vs g calculated by QMC simulation at Z_2 symmetry line with $\Delta = 9$, $L = 24$, and the Rydberg repulsive interaction truncated up to nearest-neighbor (blue triangle) and 3rd nearest-neighbor sites (red circle).

E. cavity leaking

In the experiment, the cavity-photon leakage is usually on the same order of magnitude as $\tilde{g} = g/\sqrt{N}$ [73], which gen-

	$N(V_0)+NN(V_1)$	$N(V_0)+NN(V_1)+NNN(V_2)$
Solid(1/3)-SRC I	$\tilde{\mu} = -\frac{2g^2}{3} \frac{1}{\Delta-3V_0}$	$\tilde{\mu} = -\frac{2g^2}{3} \frac{1}{\Delta-3V_0-3V_2} + 3V_2$
Solid(2/3)-SRC II	$\tilde{\mu} = \frac{2g^2}{3} \frac{1}{\Delta-3V_0-6V_1} + 6V_1$	$\tilde{\mu} = -\frac{2g^2}{3} \frac{1}{\Delta-3V_0-6V_1-3V_2} + 6V_1 + 3V_2$

TABLE II. Analytical expression of the phase boundaries solved by SCE for different truncation distances.

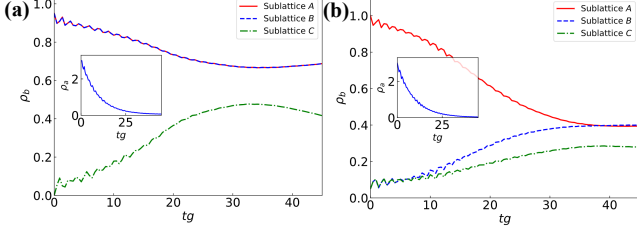


FIG. 14. The evolution of Rydberg atom density ρ_b in three sublattices and the photon density ρ_a (inset) with only cavity leakage rate $\tilde{\kappa} = \tilde{g}/3$. The initial state: (a) SRC II phase at $\tilde{\mu} = 0.3$, $g = 1.8$, (b) SRC I phase at $\tilde{\mu} = -0.2$, $g = 1.8$.

erally gives rise to non-negligible decoherence effects. To investigate whether this level of photon loss affects the stability of the SRC phases, we conduct quantum-trajectory-based simulations using QuTiP [70], an open-source Python package. Limited by computational power, we considered a 3×3 system with a photon cutoff of 8.

In Fig. 14 we present the case where only cavity-photon leakage with leaking rate $\tilde{\kappa} = \tilde{g}/3$ is considered. Fig. 14(a) shows that, within the range of our numerical simulation, the three-fold clock order of the SRC-II phase is not destroyed by cavity-photon decay. In contrast, for the SRC-I phase (Fig. 14(b)), we observe that the three-fold clock order survives only for the first several Rabi periods. After that, the Rydberg atom density in one sublattice (B) begins increasing faster than the other sublattice (C). It indicates the six-fold clock order begins to take effect, which may result from the decoherence of the photon induced by photon leakage and is consistent with the prediction of the variational approach in Fig. 6.

In the experiment, in order to suppress the strong decoherence caused by the cavity leakage, photons are usually pumped into the cavity at the same time. Here, we set the pumping rate $\zeta = \tilde{\kappa} = \tilde{g}/3$ to ensure the photon density will not decay to 0. As the result shown in Fig. 15, the three-fold clock order always survives both in SRC I and SRC II phases as the photon density ρ_a keeps a finite value during the evolution. In comparison with the no-pumping case, we can find that the coherence of the photon plays a key role in the stability of the SRC I phase.

F. tri-critical points

In the main text, we show that there are tri-critical points in the QPT between the SRC and SR phases under finite system size $L = 24$. Here, we carry out more simulations at different system sizes to figure out whether the tri-critical points will

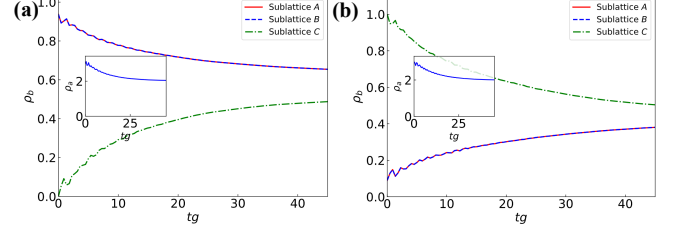


FIG. 15. The evolution of Rydberg atom density ρ_b in three sublattices and the photon density ρ_a (inset) with cavity leakage rate $\tilde{\kappa} = \tilde{g}/3$ and pumping rate $\zeta = \tilde{\kappa}$. The initial state: (a) SRC II phase at $\tilde{\mu} = 0.3$, $g = 1.8$, (b) SRC I phase at $\tilde{\mu} = -0.3$, $g = 1.8$.

merge together in the thermodynamic limit. According to the QMC simulations in Fig. 16, as the size increases, the finite-size tri-critical points gradually approach the 3D XY point. By performing a linear fitting on these $\tilde{\mu}_c$ values for the inverse of the sizes in Fig. 17, it can be observed that at the thermodynamic limit, the tri-critical points tend to merge with the 3D XY point. It indicates that the appearance of the tri-critical points is very likely to be merely a finite-size effect.

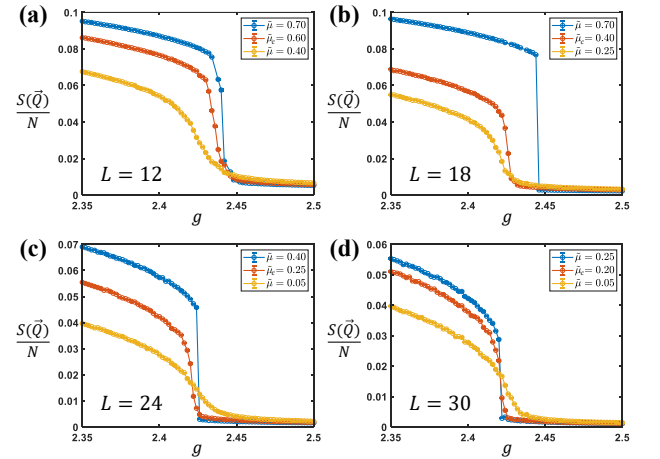


FIG. 16. The behavior of the structure factor $S(\vec{Q})/N$ near the phase boundary under different system sizes. The blue and yellow lines demonstrate the first and second order QPT between SRC II and SR phase in the finite-size system. The red lines correspond the finite-size tri-critical points, which equal $\tilde{\mu} = 0.60, 0.40, 0.25, 0.20$ for $L = 12, 18, 24, 30$.

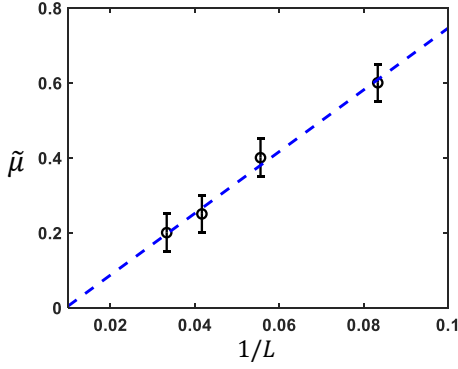


FIG. 17. Linear fitting of tri-critical points under finite sizes ($L = 12, 18, 24, 30$).

G. anisotropy parameter

Same as other frustrated systems, the irregular circle is usually due to the existence of the marginal or dangerous irrelevant terms. To provide more quantitative evidence, we take into account the anisotropy parameter $W_3 = |\cos(3 \arg(s(\vec{Q})))|$ [34]. As shown in Fig. 18, the anisotropy of $s(\vec{Q})$ near the 3D XY critical point ($g = 2.440$) approaches zero while increasing the system size. Therefore, W_3 is expected to be zero, and the histogram of $s(\vec{Q})$ can be uniformly $U(1)$ distributed in the thermodynamic limit. Definitely, our data still can not rule out the possibility of the weakly first-order QPT.

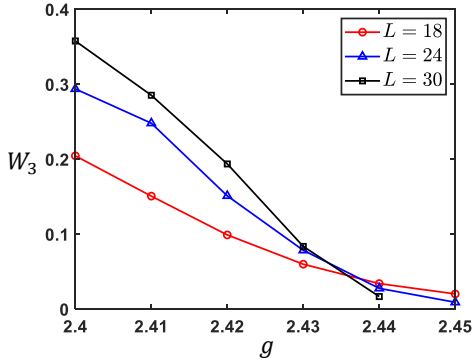


FIG. 18. The anisotropy parameter W_3 varies with g at different system sizes.

H. Inhomogeneous effect

How precisely to position the atoms at the antinode of the cavity field is a very challenging technical problem. We have found that this has been achieved quite well in a one-dimensional array [73]. They used optical tweezers to trap atoms and simultaneously utilized the blue detuning induced by the cavity light to lock the positions of the atoms more precisely, achieving a variance of the coupling strength between all atoms and the optical field within 4%. The tweezer lattice

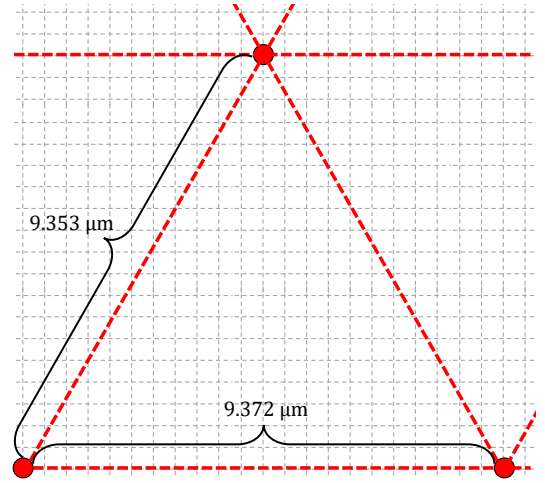


FIG. 19. A schematic diagram of the unit cell of a triangular tweezer lattice arranged on a square optical lattice with a lattice constant of $a_{\text{square}} = 0.426 \mu\text{m}$ in a cavity.

constant they provided is $8.52 \mu\text{m}$.

Assuming that the coupling variance between the atoms and the cavity field does not exceed the current experimental precision when the tweezer lattice constant is above $8.52 \mu\text{m}$, we can extend this situation to a two-dimensional square optical lattice and present a scheme for experimentally realizing a tweezer triangular lattice. Here, we set the lattice constant of this square optical lattice to be the half-wavelength of the cavity beam ($a_{\text{square}} = 0.5 \times 852 \text{nm} = 0.426 \mu\text{m}$). Thus, we can place the atoms as shown in the figure to form a tweezer triangular lattice as the Fig. 19. The three sides of the triangular unit have slight differences, and they are $a_x = 9.372 \mu\text{m}$ and $a_\Lambda = 9.353 \mu\text{m}$, respectively. This anisotropy on the tweezer lattice will lead to the anisotropy of the Rydberg interactions $V_x/V_\Lambda = a_x^6/a_\Lambda^6 = 1.012$. However, according to the result in [74], this slight anisotropy ($V_x/V_\Lambda < 1.04$) will not disrupt the order by disorder phase.

On the other hand, we also need to consider the situation where the coupling strength g is inhomogeneously distributed in space. Based on the indicators provided by the experiment, we used QMC to simulate a “disordered system” with a variance of $\pm 4\%$ for g . Specifically, we generated $N_r = 100$ replicas with g spatially uniform-random-distributed, and performed independent QMC simulations to obtain the expected values $\langle \hat{O} \rangle_i$ of the physical quantities under the specific distribution for each replica. For a disordered system, the expectation value of the observable is obtained by implementing the replica average defined as $\langle \langle \hat{O} \rangle \rangle \triangleq \sum_i \langle \hat{O} \rangle_i / N_r$. Due to the extremely large consumption of computational resources of the disordered system, we only calculated parameters $(\tilde{\mu}, g) = (0, 2.00)$ and $(\tilde{\mu}, g) = (0.20, 2.00)$ to ensure that the main conclusions of our article still hold in the disordered system. To compare with the case without disorder $\langle \hat{O} \rangle_0$, we consider such a relative change:

$$\delta_{\hat{O}} = \frac{|\langle \langle \hat{O} \rangle \rangle - \langle \hat{O} \rangle_0|}{\langle \hat{O} \rangle_0} \quad (8)$$

and we find that at $(\bar{\mu}, g) = (0.20, 2.00)$, $\delta_E = 0.00091\%$, $\delta_{\rho_b} = 0.0097\%$, $\delta_{\rho_a} = 0.65\%$, $\delta_{S(\vec{Q})} = 0.028\%$, while at $(\bar{\mu}, g) = (0, 2.00)$, $\delta_E = 0.18\%$, $\delta_{\rho_b} = 2.12\%$, $\delta_{\rho_a} = 2.99\%$, $\delta_{S(\vec{Q})} = 14.59\%$. For all the physical quantities measured above, the disorder caused by the inhomogeneous g is more pronounced on the first-order phase transition line than when it is not on. Following the same analysis in the effect of long-range interaction, the high degeneracy around the Z_2 symmetry line is strongly sensitive to a tiny energy scale, so that the disorder can bring in a large discrepancy with the pure system. However, the SRC phase is still robust against disorder.

Definitely, it does not mean the state-of-the-art experimental platform is sufficiently ready. The high-quality cavity with a large Rydberg array is still extremely challenging nowadays. However, the rapid development of the experiment always provides theoretical research with a very optimistic future. Maybe, just like the recent breakthrough on the Rydberg dressing atom in the optical lattice [67], directly trapping the Rydberg dressing atom in the triangular optical lattice in the cavity will become possible in the near future.

I. superradiant solid phase

As discussed in our previous works [78?], the superradiant solid (SRS) phases usually stay around the solid phase within a small region. Indeed, the previously observed SRS phase also exists in the triangular lattice, as the QMC simulation results in Fig. 20. The finite $S(\vec{Q})/N$ and ρ_a indicate that the translational and $U(1)$ symmetries are spontaneously broken. Meanwhile, this SRS phase follows the same mechanism in the chain and square lattice systems, which is irrelevant to the OBD algorithm.

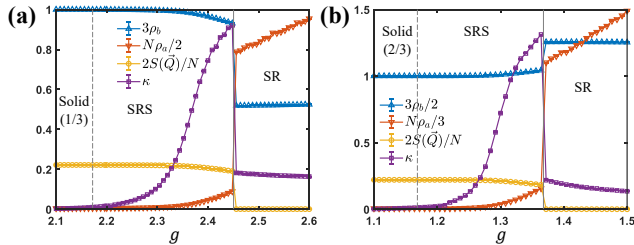


FIG. 20. The photon density ρ_a , the Rydberg atom density ρ_b , the structure factor $S(\vec{Q})$, and the compressibility κ in SRS phases near (a) solid(1/3) phase (at $\bar{\mu} = -2.75$) and (b) solid(2/3) phase (at $\bar{\mu} = 2.80$). The dash (solid) line marks the second (first) order QPT. The data are simulated by the QMC at $L = 24$ and $\Delta = 9$.

J. Topological sector

As emphasized in the introduction, the strong Rydberg interactions and geometric frustration lead to a disordered

ground state with high macroscopic degeneracy, which is related to the topological sectors. Here, we would like to make it clearer. As shown in Fig.21(a), around the Z_2 symmetry line, empty and full triangles (fractional charges in lattice gauge theory) are forbidden or gaped according to the triangle constraint. Then, the restricted Hilbert space satisfying the triangle rule can be separated into different topological sectors with a different number of the degeneracy. The topological sector can be labeled by the winding numbers N_W , which equals the number of antiferromagnetic bonds in each direction (here only the x component is considered) [77]. The simplest one is the stripe phase illustrated in Fig.21(b) with $N_W = 0$ and its degeneracy being one.

Then, as demonstrated in Fig.21(c), after altering all the configurations in the right part (by surface operator), one domain wall is introduced, and the system enters into the topological sector with $N_W = 1$. We observe that exchanging the local configurations (such as spin exchanges) within the blue circle does not violate the triangular constraint. This implies that the associated topological sector remains unchanged, and consequently, the corresponding degeneracy exceeds that of the stripe phase. Because both three- and six-fold clock terms favor the same topological sector with $N_W = 2L_x/3$, the winding number during the QPT between SRC and solid phase should be unchanged. Furthermore, as shown in Fig.21(e), because the fractional charges are confined, the fractional charge pair with only a short distance can be excited at low temperature due to the quantum and thermal fluctuations.

As the comparison in Fig.22, the winding number during the QPT from the solid to the SRS phase is smoothly changed, which means the ground state of the SRS phase has no relation with the topological sector, otherwise a clear staircase would be expected as the TIM or XXZ model [74, 76? , 77]. Differently, as shown in the left side of Fig.22, the winding number during the QPT between the solid and SRC phase is almost unchanged and very close to $2L_x/3$, just the same as the prediction.

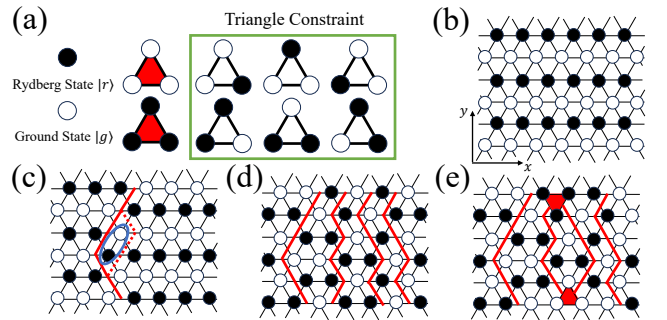


FIG. 21. Schematic diagrams related to the topology. (a) Triangle constraint with fractional charge (red triangle); (b) Configuration of stripe order with winding number $N_W = 0$; (c) Configuration of single domain wall (red line) which can be changed to new shape (dashed red line) without changing $N_W = 1$ by local exchange interaction (blue circle); (d) Configuration of SRC phase with $N_W = 2L_x/3$; (e) Possible fractional excitation at high temperature.

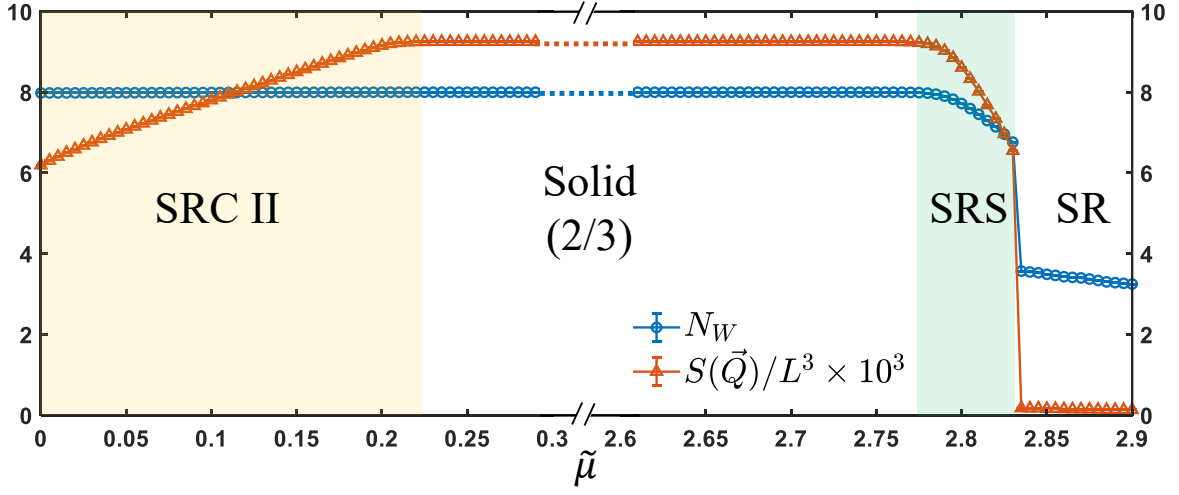


FIG. 22. The winding number N_W and the structure factor $S(\vec{Q})/N$ vs $\tilde{\mu}$ at $g = 1.30$. The SRC phase(left) and the SRS phase(right) determined by $S(\vec{Q})/N$ are marked with yellow and green background, respectively. The data are simulated by the QMC at $L = 12$ and $\Delta = 9$.